

## RESEARCH ARTICLE

# Data-driven algorithm for myelin water imaging: Probing subvoxel compartmentation based on identification of spatially global tissue features

Noam Omer<sup>1</sup> | Meirav Galun<sup>2</sup> | Neta Stern<sup>1</sup> | Tamar Blumenfeld-Katzir<sup>1</sup> |  
Noam Ben-Eliezer<sup>1,3,4</sup> 

<sup>1</sup>The Department of Biomedical Engineering, Tel-Aviv University, Tel Aviv, Israel

<sup>2</sup>Department of Computer Science and Applied Mathematics, Weizman Institute of Science, Rehovot, Israel

<sup>3</sup>Sagol School of Neuroscience, Tel-Aviv University, Tel-Aviv, Israel

<sup>4</sup>Center for Advanced Imaging Innovation and Research (CAI2R), New York University Langone Medical Center, New York, New York, USA

## Correspondence

Noam Ben-Eliezer, The Department of Biomedical Engineering, Tel Aviv University, Tel Aviv 6997801, Israel  
Email: noambe@tauex.tau.ac.il

## Funding information

Israeli Science Foundation, Grant/Award Number: 2009/17

## Abstract

**Purpose:** Multicomponent analysis of MRI  $T_2$  relaxation time ( $mcT_2$ ) is commonly used for estimating myelin content by separating the signal at each voxel into its underlying distribution of  $T_2$  values. This voxel-based approach is challenging due to the large ambiguity in the multi- $T_2$  space and the low SNR of MRI signals. Herein, we present a data-driven  $mcT_2$  analysis, which utilizes the statistical strength of identifying spatially global  $mcT_2$  motifs in white matter segments before deconvolving the local signal at each voxel.

**Methods:** Deconvolution is done using a tailored optimization scheme, which incorporates the global  $mcT_2$  motifs without additional prior assumptions regarding the number of microscopic components. The end results of this process are voxel-wise myelin water fraction maps.

**Results:** Validations are shown for computer-generated signals, uniquely designed subvoxel  $mcT_2$  phantoms, and in vivo human brain. Results demonstrated excellent fitting accuracy, both for the numerical and the physical  $mcT_2$  phantoms, exhibiting excellent agreement between calculated myelin water fraction and ground truth. Proof-of-concept in vivo validation is done by calculating myelin water fraction maps for white matter segments of the human brain. Interscan stability of myelin water fraction values was also estimated, showing good correlation between scans.

**Conclusion:** We conclude that studying global tissue motifs prior to performing voxel-wise  $mcT_2$  analysis stabilizes the optimization scheme and efficiently overcomes the ambiguity in the  $T_2$  space. This new approach can improve myelin water imaging and the investigation of microstructural compartmentation in general.

## KEYWORDS

multicomponent  $T_2$  relaxation analysis, myelin water fraction, myelin water imaging, subvoxel compartmentation

## 1 | INTRODUCTION

Biological tissues have a complex microstructure, which is challenging to probe *in vivo*. Notwithstanding its high clinical value, MRI is limited in visualizing tissues microstructure due to a hard limit on achievable resolutions. Recent studies have shown that this limitation can be partially circumvented by modeling the MRI signal as consisting of several water pools, each residing in a distinct magnetochemical environment.<sup>1</sup> The measured MRI signal is thus considered to reflect a spatiotemporal average over several water pools and over time. In tissues where microstructural order exists, it is possible to identify a finite number of specific water pools (i.e., tissue compartments), each producing a signal that is proportional to the relative amounts of water in that compartment. By deconvolving the signal into its underlying components, it is thus possible to indirectly probe the tissue's subvoxel compartmentation. An example of such ordered tissue, and the focus of this study, is the brain white matter (WM). This tissue is typically modeled to have 3 distinct water pools: intra-axonal water, extra-axonal water, and water that reside between myelin sheaths.<sup>1</sup> Estimating the relative myelin water fraction (i.e., myelin water imaging [MWI]<sup>2,3</sup>) is of the high interest because it reflects the local myelin content<sup>4,5</sup>—a valuable biomarker for myelodegenerative disorders<sup>6,7</sup> and neuronal developmental processes.<sup>8,9</sup>

An effective approach for probing subvoxel compartments is multicomponent analysis of MRI transverse  $T_2$  relaxation time (mc $T_2$ ).<sup>10–12</sup> This approach leverages the fact that  $T_2$  relaxation times vary between compartments and also that its spectral profile ( $T_2$  spectrum) changes in presence of pathology.<sup>3</sup> In the case of WM, mc $T_2$  is based on the difference in  $T_2$  between water pool that reside between myelin sheaths (1–40 ms) and the extra-/intra-water pools (>50 ms).<sup>2,3</sup> Therefore, when interpreting the  $T_2$  spectrum of WM voxel, the relative amount of myelin water can be estimated by dividing the area under the pool with the shortest  $T_2$  by the area of the entire spectrum. This ratio is known as myelin water fraction (MWF).<sup>13,14</sup> Applications mc $T_2$  analysis have already been shown, for example, in multiple sclerosis, where myelin loss may be detected through a reduction in the short  $T_2$  component,<sup>15</sup> or in Alzheimer disease, where demyelination was found to correlate with cognitive decline.<sup>16</sup>

The most efficient pulse sequence for extracting mc $T_2$  data is the classical Hahn spin echo. This acquisition scheme, however, involves extensive scan times, making rapid multi-echo spin echo (MESE) protocols the most practical *in vivo* alternative. Other approaches for mc $T_2$  use fast multi-echo acquisition schemes, which combine multiple gradient echoes per spin echo,<sup>17</sup> multicomponent driven equilibrium single pulse observation of  $T_1$  or  $T_2$ ,<sup>18,19</sup> and MR fingerprinting.<sup>20,21</sup> Still, these gradient-echo based methods have not supplanted the established multi-spin echo methods for mc $T_2$  relaxometry,<sup>22,23</sup> mainly due to their reduced  $T_2$  encoding efficiency.

Traditionally, mc $T_2$  analysis of MESE data considers the signal to be a weighted sum of mono-exponential decay curves, allowing the use of discrete Fredholm integral equation (i.e., inverse Laplace transforms) for producing the  $T_2$  spectrum:

$$S(t_i) = \sum_{m=1}^M w_m \cdot \exp(-t_i/T_{2,m})^\infty + \eta(t_i) \quad i = \{1, 2, \dots, \text{ETL}\}. \quad (1)$$

Here,  $S$  is the measured signal at a given voxel;  $t_i$  is a discrete time axis ranging from the first to echo train length time points;  $M$  is the number of signal components associated with tissue compartments,  $w_m$  and  $T_{2,m}$  are the amplitude and relaxation time of component  $m$ , respectively; and  $\eta$  is a noise term. A straightforward solution of this problem can be achieved using nonnegative least squares (NNLS)-fitting algorithm.<sup>24</sup> Several improvements of the basic NNLS approach have been suggested, mostly by adding regularization terms to stabilize the fitting process and by modeling the  $T_2$  spectrum as a discrete rather than continuous series of values.<sup>25,26</sup> Other techniques assume an a priori fixed number of 2 or 3 compartments for the WM or exploit spatial correlations between adjacent voxels.<sup>27,28</sup> Notwithstanding the advantages of the above techniques, they produce different values, which moreover vary between scanner and scan settings, leading to a lack of a gold standard MWI technique.<sup>12,23</sup> The key challenge in this case is the inherent ambiguity of the multiparametric mc $T_2$  space, which has a potentially large number of possible microstructural configurations that can match a certain experimental decay curve. The result is a highly underdetermined and ill-posed problem whose solution suffers from non-uniqueness and sensitivity to noise.<sup>29</sup> Regularization alleviates some of the ill-posedness of the

problem; however, it does not ensure convergence or validity of the ensuing solution.

In this study, we introduce a new  $mcT_2$  approach, which employs a statistical preprocessing stage to identify spatially global  $mcT_2$  motifs of the tissue. These motifs consist of a subset of  $mcT_2$  patterns, which are common to the brain segment being analyzed. Once identified, the motifs are used to locally analyze the signal at each voxel while still imposing standard regularization constraints. Eventually, each voxel is associated with a unique  $T_2$  spectrum and MWF value. The statistical power produced by this data-driven approach endows the whole process with additional robustness, which stabilizes the voxel-wise optimization scheme. Another strength of this approach stems from the use of the echo-modulation curve (EMC) technique.<sup>30–32</sup> By incorporating the exact scan settings and protocol implementation into its signal model, this technique is able to overcome the contamination of MESE signals by stimulated and indirect echoes and produce accurate  $T_2$  values that are reproducible across scanners and scan settings.<sup>31</sup> The accuracy of the proposed  $mcT_2$  approach is demonstrated on numerical and physical phantoms, followed by feasibility of applying this technique on WM brain tissue in vivo.

## 2 | THEORY

Multicomponent  $T_2$  decay curves consist of a linear combination of single  $T_2$  signals originating from microscopic subvoxel compartments. Previous studies have shown that tissues with ordered internal structure can be modeled using a discrete and finite set of compartments with distinct  $T_2$  values.<sup>12,28</sup> Accordingly, we adopt here a common model for myelinated WM tissue consisting of up to 3 signal sources: (i) water trapped between myelin sheaths (fast-relaxing component), (ii) intra-axonal water, and (iii) extra-axonal water.<sup>33</sup> The new  $mcT_2$  signal analysis approach suggested herein is furnished with several unique features. First, unlike traditional approaches that analyze data from a single voxel, we start by identifying regional  $mcT_2$  motifs from an entire brain segment and only then focus on deconvolving the signal from each voxel. Secondly, we allow the existence of either 1, 2, or 3  $T_2$  compartments within each voxel without imposing a fixed number or distribution of compartments. Third, we do not rely on an exponential decay but instead base our analysis on the EMC signal model. Incorporating this model into (1) yields:

$$s(t_i) = \sum_{m=1}^M w_m \cdot \text{EMC}(T_{2,m}, t_i) + \eta(t_i) \quad i = \{1, 2, \dots, \text{ETL}\}. \quad (2)$$

The numerical term  $\text{EMC}(T_{2,m}, t_n)$  denotes a single  $T_2$  decay curve out of a dictionary of possible curves. Equation (2) can be cast into a linear matrix form:

$$S = \mathbf{E}w + H, \quad (3)$$

where  $S \in \mathbb{R}^{\text{ETL} \times 1}$  is the experimentally measured signal from a single voxel;  $\mathbf{E} \in \mathbb{R}^{\text{ETL} \times N_{T_2}}$  is a simulated dictionary of single- $T_2$  EMC signals expected to appear in the tissue;  $w \in \mathbb{R}^{N_{T_2} \times 1}$  is an unknown weights vector representing the relative fractions of the elements in  $\mathbf{E}$ ; and  $H \in \mathbb{R}^{\text{ETL} \times 1}$  is an unknown noise vector. Straightforward inversion of this system of equations is computationally intractable due to the large number of possible combinations and noise related ambiguity, both which lead to unstable solutions. To overcome this inherent ill-posedness, we precede the solution to (3) with an important preprocessing step whereby we identify a basis set of  $mcT_2$  motifs that best describe the entire WM segment. This subset of  $mcT_2$  motifs, which were generated from weighted linear combinations of the single  $T_2$  signals in  $\mathbf{E}$ , is used as a new basis to deconvolve the local signal within each voxel.

### 2.1 | Identification of a basis set of global $mcT_2$ signal motifs

Identifying the tissue-specific set of  $mcT_2$  motifs is based on the premise that *only a finite number of microstructural configurations exist within each tissue segment*. This process is done in 2 stages: first, a broad  $mcT_2$  dictionary is generated that contains all possible permutations of  $T_2$  values and fractions. This extensive set of configurations is then narrowed down to a small and finite set of motifs using statistical correlation with the measured data. We note that separate dictionary should be created for each scan settings. This, however, does not pose a serious limitation because the same dictionary can be used for varying FOVs and matrix sizes once the protocol is stabilized.

The full range of possible microstructural tissue configurations is constructed by combining sets of single  $T_2$  signals, logarithmically spaced between 1 ... 800 ms, thereby covering the physiological range of  $T_2$  values (Figure 1(1)). This results in a dictionary of  $mcT_2$  motifs  $\mathcal{D} \in \mathbb{R}^{\text{ETL} \times N_{mcT_2}}$  having  $N_{mcT_2}$  elements, each consisting of linear combination of single  $T_2$  components with varying fractions (Figure 1(2)). The transformation operator between single- to multi-component dictionary is denoted by a coefficient matrix  $\mathcal{D} \in \mathbb{R}^{\text{ETL} \times N_{mcT_2}}$   $\mathbf{W} \in \mathbb{R}^{N_{T_2} \times N_{mc}}$ , with rows representing the relative fractions of each single  $T_2$  component ( $w$ ) and the columns representing all possible combinations. Put in matrix form, this becomes:

$$\mathcal{D} = \mathbf{E}\mathbf{W} \text{ s. t. } \forall i \sum_{j=1}^{N_{T_2}} w_{i,j} = 1; \forall i, j \quad 0 \leq w_{i,j} \leq 1, \quad (4)$$

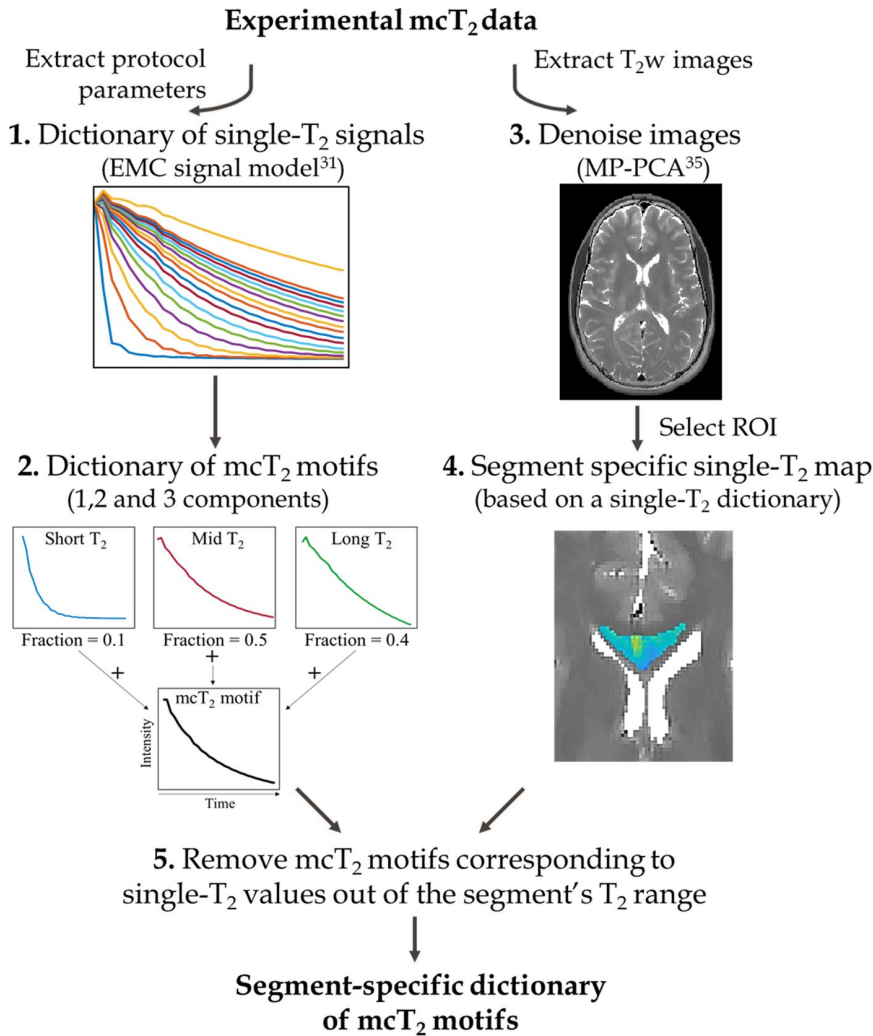


**FIGURE 1** A flowchart describing the creation of a data-driven dictionary of mcT<sub>2</sub> motifs for a selected brain segment. (1) Multi-component T<sub>2</sub> signals (mcT<sub>2</sub>) are acquired, whereas the corresponding scan parameters are extracted and inputted into the echo-modulation-curve signal model<sup>30</sup> to produce a dictionary of simulated single T<sub>2</sub> signals. (2) This dictionary is first used to create an expanded dictionary of mcT<sub>2</sub> motifs by combining 1, 2, and 3 single T<sub>2</sub> signals with varying weights according to the physiological range of microstructural tissue configurations. (3) Experimental mcT<sub>2</sub> data is denoised using a PCA-based denoising scheme.<sup>34</sup> (4) Denoised data from a specific brain region (ROI) is used to generate a map of single T<sub>2</sub> values. (5) The range of the single T<sub>2</sub> values within the segment is used to filter out mcT<sub>2</sub> motifs that do not average to a T<sub>2</sub> value that matches to the segment's T<sub>2</sub> range. mcT<sub>2</sub>, multi-component T<sub>2</sub> signals; ROI, region of interest

where we note that the sum of weights for each mcT<sub>2</sub> combination needs to be one, and that fraction values are in the range of 0 ... 1. The number of elements in the mcT<sub>2</sub> dictionary ( $N_{\text{mcT}_2}$ ) increases dramatically with the number of T<sub>2</sub> values ( $N_{\text{T}_2}$ ), and the step size of the relative fraction of each component ( $\Delta w$ ). The final number of elements can be calculated using the following combinatorial sum:

$$N_{\text{mcT}_2} = \underbrace{\binom{N_{\text{T}_2}}{1}}_{\text{one-comp.}} + \underbrace{\binom{N_{\text{T}_2}}{2} \left(\frac{1}{\Delta w} - 1\right)}_{\text{two-comp.}} + \underbrace{\frac{1}{2} \binom{N_{\text{T}_2}}{3} \left(\frac{1}{\Delta w} - 2\right)^2 \left(\frac{1}{\Delta w} - 3\right)}_{\text{three-comp.}}, \quad (5)$$

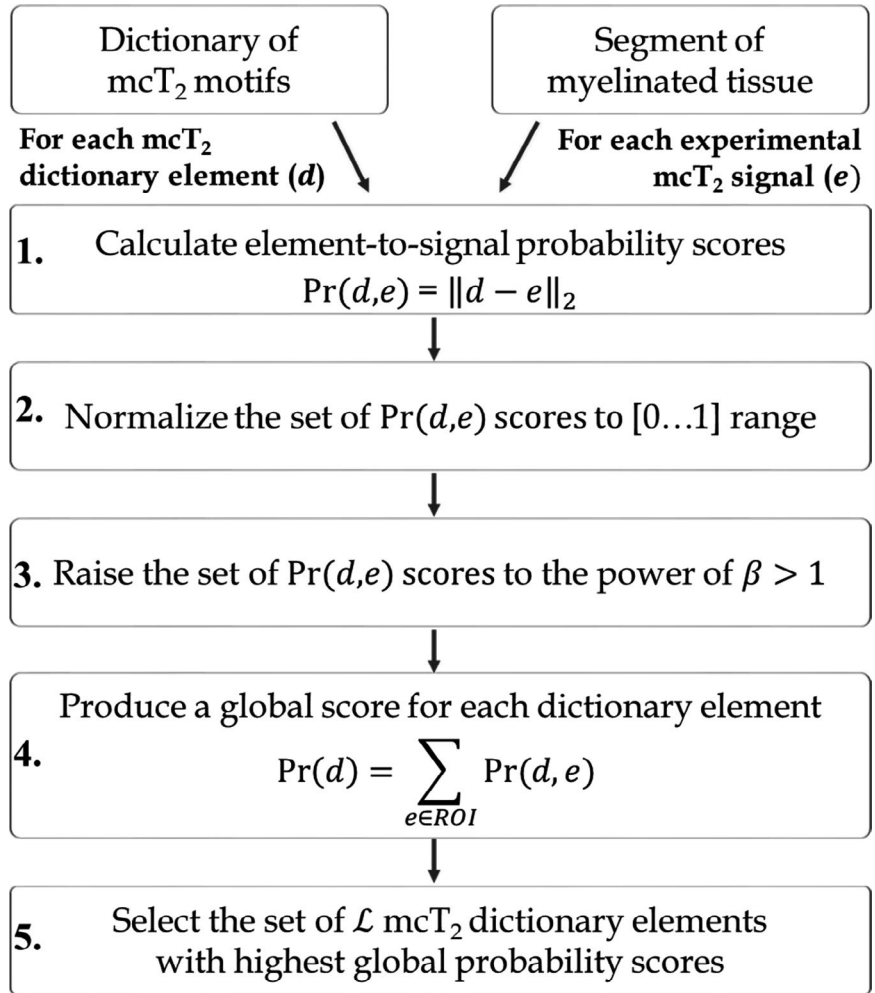
resulting, for example, in 4 401 475 elements for 1–3 subvoxel compartments, 50 T<sub>2</sub> values, and  $\Delta w = 0.1$ . It is important to emphasize that each mcT<sub>2</sub> dictionary element also has a single T<sub>2</sub> value associated with it, calculated analytically as the weighted average of the single T<sub>2</sub> values from the different subvoxel compartments. The method benefits from the fact that some mcT<sub>2</sub> dictionary elements have single T<sub>2</sub> values that do not exist in the analyzed tissue segment (Figure 1(4)). By performing a single T<sub>2</sub> fit of our data, we narrow down

the number of mcT<sub>2</sub> elements by removing all dictionary elements whose single T<sub>2</sub> value do not fall within a 10% of the range of T<sub>2</sub> values found in this segment (20% was used for T<sub>2</sub>s < 30 ms) (Figure 1(5)). This is done in 3 stages: (i) For each single T<sub>2</sub> value in the segment, we identify a range of  $\pm 10\%$  around it (20% for T<sub>2</sub> ≤ 30); (ii) all ranges are consolidated into a global range single T<sub>2</sub> values appearing in the tissue; (iii) we exclude dictionary elements which are averaged to single T<sub>2</sub> values outside this set. De facto this step removed almost half of the initial number of mcT<sub>2</sub> dictionary elements.

Once an mcT<sub>2</sub> dictionary is available, the statistical correlation between each dictionary element ( $d$ ) and experimental signal ( $e$ ) is calculated based on the L<sub>2</sub> norm difference between each pair (Figure 2(1)). This provides a pairwise score value  $\text{Pr}(d,e)$ , which is normalized to [0 ... 1] (Figure 2(2)). This score is subsequently raised to the power of  $1 \leq \beta < 10^4$  to prioritize mcT<sub>2</sub> motifs that have higher probability to be found within the segment (Figure 2(3))—even if they match well with only a small number of voxels (e.g., for modelling focal lesion points within the analyzed segment). Finally, the score of each dictionary element ( $d$ ) is summed across all voxels (Figure 2(4)) to



**FIGURE 2** The process of identifying spatially global  $mcT_2$  motifs of myelinated tissues. (1) A correlation-based score is computed between each experimental signal “ $e$ ” and  $mcT_2$  dictionary element “ $d$ ” to produce a set of probability scores  $Pr(d,e)$ . (2,3) Scores are normalized and raised by power of  $\beta$  to prioritize  $mcT_2$  motifs according to their probability to be found within the segment while still retaining selected motifs that have high correlation with only a small number of voxels. (4) Sum the scores of each dictionary element across all signals to produce a global score  $Pr(d)$  for each dictionary element. (5) Select a finite group of  $\mathcal{L}$  dictionary elements with the highest scores



form a global, element-specific, probability score  $Pr(d)$ . We note the important role of the  $\beta$  parameter, which is to ensure that  $mcT_2$  motifs with very high scores, that is, which perfectly match a small number of the voxels in the segment, will maintain their high score when summing the scores of all voxels. This, for example, can happen when small focal pathology appears within the segment.

To exclude low SNR signal points, we precede these calculations by normalizing the signal (dividing by the first time point) and truncating data points at the tail of the signal below a 0.1 threshold. Excluding low SNR data points removes any bias caused by Rician noise and leaves  $H$  with only Gaussian noise distribution.<sup>35</sup> Following the calculation of all scores, a segment-specific set of  $\mathcal{L}mcT_2$  motifs is selected having the highest scores, that is, the  $mcT_2$  dictionary elements with highest probability to be found within the segment (Figure 2(5)). Denoting this group of  $\mathcal{L}$  elements as  $E \in \mathbb{R}^{ETL \times \mathcal{L}}$ , we can substitute the term  $Ew$  in (3) and express the signal at each voxel as a sum of  $mcT_2$  motifs:

$$S = EW + H \quad (6)$$

where  $W \in \mathbb{R}^{\mathcal{L} \times 1}$  is the unknown weights of each motif in  $E$ .

## 2.2 | Calculating each voxel's $mcT_2$ content

To solve (6), we cast it as minimization problem with the following objective function:

$$\underset{W}{\operatorname{argmin}} \Phi = \frac{1}{2} \|EW - S\|_2^2 + \lambda_{\text{Tik}} \|W\|_2^2 + \lambda_{L_1} \|W\|_1 \quad (7)$$

$$s. t. W_i \geq 0, \quad \sum W_i = 1.$$

Here,  $S \in \mathbb{R}^{ETL \times 1}$  is the measured signal, and  $\lambda_{\text{Tik}}, \lambda_{L_1} > 0$  are Tikhonov and  $L_1$  regularization weights. The Tikhonov regularization is added to guarantee a well-posed problem, and the  $L_1$  regularization is added in order to favor sparse  $T_2$  distributions. The regularization weights of the objective function are determined based on an exhaustive search in the range  $10^{-7} \dots 10^{+7}$ , ensuring optimal performance and stability (see Table 1). The last 2 constraints ensure that the solution vector  $W$  is nonnegative and forces its sum to be unity. Equation (7) was solved using MatLab's *quadprog* solver (version 2019b) for quadratic objective functions with linear constraints (MathWorks, Natick, MA). This solver finds a minimum for problems specified by the standard form of quadratic programming:

TABLE 1 List of optimal parameters for the suggested mcT<sub>2</sub> algorithm

Parameter	Dictionary Elements <sup>a</sup>	Single T <sub>2</sub> Elements <sup>b</sup>	mcT <sub>2</sub> Motifs Expected in Segment	Fractional T <sub>2</sub> Weighting <sup>c</sup>	Prioritization Factor	Tikhonov Reg. Weight	L <sub>1</sub> Reg. Weight	Natural T <sub>2</sub> Variation Allowed in Segment <sup>d</sup>
Symbol	N <sub>mcT<sub>2</sub></sub>	N <sub>T<sub>2</sub></sub>	$\mathcal{L}$	$\Delta\omega$	$\beta$	$\lambda_{\text{Tik}}$	$\lambda_{\text{L1}}$	T <sub>2</sub> <sup>thr</sup>
Numerical simulation	3 273 304	64	50	0.1	10 <sup>3</sup>	10 <sup>-3</sup>	10 <sup>3</sup>	0.1–0.2
Expr. phantom	1 306 597	50	30	0.05–0.1	10 <sup>2</sup>	10 <sup>-3</sup>	10 <sup>3</sup>	0.1–0.2
In vivo scan	3 273 304	64	30	0.05–0.1	10 <sup>4</sup>	10 <sup>-2</sup>	10 <sup>3</sup>	0.1–0.2

Abbreviations: Expr., experimental; mcT<sub>2</sub>, multi-component T<sub>2</sub> signals.

<sup>a</sup>The number of elements in the dictionary of mcT<sub>2</sub> motifs comprising of 1, 2, and 3 single T<sub>2</sub> components.

<sup>b</sup>The number of single T<sub>2</sub> values ranging logarithmically between 1 and 800 ms used for creating the simulated dictionary of mcT<sub>2</sub> motifs.

<sup>c</sup>Water pool fractions were set at jumps of  $\Delta\omega = 0.05$  for T<sub>2</sub> ≤ 40 ms, and  $\Delta\omega = 0.1$  for T<sub>2</sub> > 40 ms.

<sup>d</sup>Natural variation in T<sub>2</sub> values of ±10% was imposed for T<sub>2</sub> ≤ 30 and ±20% for T<sub>2</sub> > 30.

$$\min_x \frac{1}{2} x^T H x + f^T x. s. t. \begin{cases} Ax \leq b \\ A_{eq} x = b_{eq} \\ lb \leq x \leq ub \end{cases}, \quad (8)$$

where  $H \succcurlyeq 0$  represents a semi-positive definite matrix;  $f$  represents a linear term; and  $x$  denotes a vector of unknowns. To use this quadratic programming solver, we rearrange the terms in (7) and add a set of slack variables. These steps are described in detail in the Supporting Information (S4).

MatLab's (MathWorks, version 2019b) quadratic programming solver of (8) produces a solution  $x$  containing  $2 \times \mathcal{L}$  variables, out of which we are only interested in the first  $\mathcal{L}$ , which represent the elements in  $\mathbb{W}$ . We remember that these weights are used to extract the experimental signal from the  $\mathbb{E}$  matrix of mcT<sub>2</sub> motifs (see (6)). Recovering the actual voxel-specific mcT<sub>2</sub> spectrum, that is, the weights vector  $w$  from (3), is performed in 2 steps. First, we extract  $\mathbf{W}_{\mathcal{L}} \in \mathbb{R}^{N_{T_2} \times \mathcal{L}}$  by identifying the columns in  $\mathbf{W}$ , the coefficient matrix containing all possible permutations of multi-T<sub>2</sub> fractions associated with the  $\mathcal{L}$  selected mcT<sub>2</sub> motifs. We then multiply each column in  $\mathbf{W}_{\mathcal{L}}$  by its matching weight in  $\mathbb{W}$  and sum across columns to obtain the final weights vector  $w$ . This step is similar to calculating  $w = \mathbf{W}_{\mathcal{L}} \mathbb{W}$ .

MatLab's (MathWorks) quadratic programming allows input of an initial solution to the optimization process. To utilize this feature, we perform 2 iterations of the optimization procedure.<sup>7–20</sup> The first is preceded by a preprocessing step for which a 2D moving average window of  $3 \times 3$  voxels is applied to all images in order to increase SNR on expense of blurring the spatial features. The output from this iteration is then input as an initial guess to the second iteration, which uses the original images (without averaging), thereby retaining the original spatial resolution.

## 3 | METHODS

### 3.1 | Numerical phantom simulations

The mcT<sub>2</sub> signal motifs of 5 myelinated tissues and 1, 2, and 3 compartments were simulated for a range of myelin water fractions of 0%–20% (T<sub>2</sub> = 10–40 ms) and intra-/extracellular water compartments (T<sub>2</sub> = 50–80 ms). Figure 3 illustrates the numerical phantom design. The suggested data-driven mcT<sub>2</sub> algorithm was applied to the simulated data (parameters values are detailed in Table 1 and above). To estimate its accuracy when using standard voxel-wise NNLS fitting algorithm, we have implemented the state-of-the-art regularized NNLS inversion algorithm by Provencher,<sup>36</sup> which was used in the landmark publication by Whittall and MacKay.<sup>24</sup>

Prior to the analysis, Gaussian noise at SNR of 200, 100, 60, 40, and 25 was added to the signal. Next, MWF values were calculated from the reconstructed spectra by summing the area under the peak in the short  $T_2$  range ( $0\text{--}40\text{ ms}$ )<sup>2</sup> and then compared between both methods. The sum of the final weights vector was normalized to 1, meaning that this area directly reflected the MWF value. The exact set of parameters that was used for the voxelwise NNLS fitting algorithm can be found in the Supporting Information Data S3.

### 3.2 | Experimental phantom preparations

Two physical mcT<sub>2</sub> phantoms, consisting of 2 and 3 subvoxel compartments, were prepared. Each phantom consisted of a varying number of 1 mm tubes that were gradually inserted into a 5 mm tube. The dimensions allowed the entire phantom to be captured within a single imaged voxel, and at the same time they enabled high-resolution imaging, which provided ground truth of the  $T_2$  values and fractions of each compartment (see Figure S1). Fourteen 1 mm tubes with  $T_2 = 11\text{ ms}$  represented myelin water. Six 1 mm tubes with  $T_2 = 80\text{ ms}$  represented

the extra-axonal water pools. These were prepared by mixing  $\text{MnCl}_2$  and double distilled water at different concentrations. The two 5 mm holding tubes were filled with solutions having  $T_2 = 60$  and  $51\text{ ms}$  for the 2 and 3 compartments, respectively. Phantoms were scanned in a dynamic manner by gradually inserting 1 mm tubes into the 5 mm holding tubes and imaging each phase of the phantom. Eight 1 mm tubes ( $T_2 = 11\text{ ms}$ ) were inserted, 1 at a time, into the two-compartment holding tube; and twelve 1 mm tubes ( $T_2 = 51$  and  $80\text{ ms}$ ) into the three-compartment tube. The low-resolution mcT<sub>2</sub> data of each scan served as input for the mcT<sub>2</sub> fitting algorithm with the MWF calculated according to relative area of the short- $T_2$  peak ( $0\text{--}40\text{ ms}$ )<sup>2</sup>. Ground truth MWF values were calculated from the corresponding high-resolution scans based on the relative area of the short  $T_2$  tubes. Pearson correlation was calculated between the actual and estimated MWF to assess the statistical correlation.

### 3.3 | Phantom MRI scans

Phantom MESE scans were performed on 9.4 Tesla (Bruker BioSpec) using a single channel transceiver coil. A series

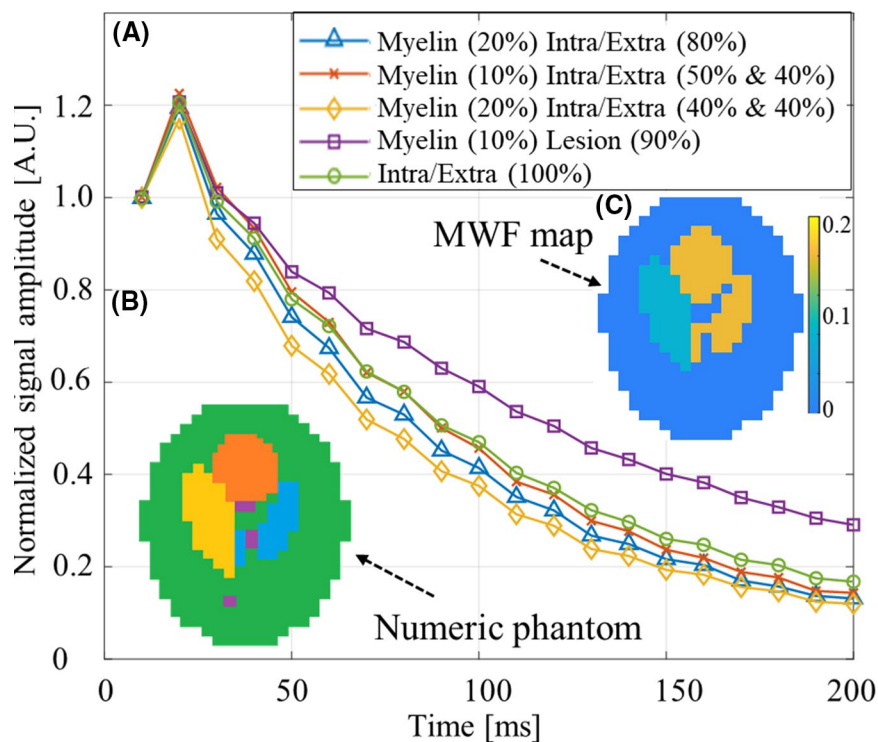


**FIGURE 3** Numerical phantom design for modeling myelinated brain tissue. A series of simulated mcT<sub>2</sub> signals motifs were produced based on clinical MESE protocol parameters and arranged in a 2D numerical Shepp-Logan phantom design. (A) The simulated tissue contains 5 ensembles simulated single  $T_2$  signals weighted by different  $T_2$  fractions associated with myelinated brain tissue composition (exact fractions are listed within the figure). (B) 2D display of the Shepp-Logan phantom presenting the distribution of the 5 mcT<sub>2</sub> motifs within the segment with different colors. Prior to analysis, white Gaussian noise was added to the numerical signals at different SNR = {200, 100, 60, 40, 25}. (C) The MWF map of the numerical phantom in B. MESE, multi-echo spin echo, MWF, myelin water fraction.

of scans were performed with varying internal configuration of the phantom, each involving a high-resolution scan (voxel size =  $156 \times 156 \mu\text{m}^2$ ) and a low-resolution scan (voxel size =  $5 \times 5 \text{mm}^2$ ). Whereas the low-resolution scan captured the entire phantom within a single voxel and produced a genuine  $\text{mcT}_2$  signal, the high-resolution scan provided reliable ground truth information about the  $T_2$  values within each compartment. Phantoms were scanned at several configurations, each time with increasing fraction of the short  $T_2$  components (see Figure 5) based on the relative area of the short  $T_2$  capillaries tubes.

To further increase the number of low-resolution slices, each scan was repeated 9 times with varying slice offsets, producing a total of 81  $\text{mcT}_2$  signals (black lines in Figure S1). The remaining experimental parameters were  $N_{\text{averages}} = 4$ ,  $\text{TR} = 5000 \text{ms}$ ,  $\text{TE} = 8, 16, \dots, 240 \text{ms}$  ( $N_{\text{TE}} = 30$ ), slice thickness = 0.8 mm, acquisition bandwidth = 50 kHz, and slice gap = 150%. The  $\text{mcT}_2$  data was fitted using a dictionary composed of 50 single  $T_2$  signals, logarithmically spaced between 1–800 ms and fraction resolution of  $\Delta\omega = 0.05$  for  $T_2 \leq 40 \text{ms}$  and  $\Delta\omega = 0.1$  for  $T_2 > 40 \text{ms}$ . This resulted in a dictionary of 1 306 597  $\text{mcT}_2$  motifs, which were narrowed to ~600 000 elements based on their single  $T_2$  values. Statistical correlations between dictionary elements and each pixel signals were calculated ( $\text{Pr}(d,e)$ ), and the resulting set of scores was normalized and raised by a power of  $\beta = 10^2$ . Scores were then summed across all pixels to obtain a global probability score ( $\text{Pr}(d)$ ), and a set of  $\mathcal{L} = 30$  dictionary elements with highest probabilities was selected as basis set of  $\text{mcT}_2$  motifs ( $\mathbb{E}$ ). Table 1 lists the full set of parameters values. Because all the slices are expected to produce the same  $\text{mcT}_2$  spectra, MWFs of each compartment were averaged across all slices.

### 3.4 | In vivo brain MRI scans

In vivo brain scans were performed on a 3 Tesla whole body MRI scanner (Prisma, Siemens Healthineers) using a 24-channel head coil. Scans were performed according to Helsinki ethical standards. To test the  $\text{mcT}_2$  fitting reproducibility, 3 identical MESE scans were performed for the same subject during 1 scan session. The subject was a 31-year-old healthy male with normal body mass index. Experimental parameters were  $\text{FOV} = 200 \times 210 \text{cm}$ , matrix size =  $216 \times 180$ ,  $N_{\text{AVERAGE}} = 1$ ,  $\text{TR} = 3000 \text{ms}$ ,  $\text{TE} = 10, 20, \dots, 200 \text{ms}$  ( $N_{\text{TE}} = 20$ ), slice thickness = 3 mm, and acquisition bandwidth = 210 Hz/Px. To improve data SNR, an image denoising step was applied to the raw images using the algorithm described in Ref.<sup>34</sup> Three WM segments were investigated: the genu corpus callosum (GCC), splenium of corpus callosum (SCC), and a left for-ceps minor segment containing 201 227 and 475 voxels,

respectively. Segments data were analyzed with an  $\text{mcT}_2$  dictionary containing 64 elements, logarithmically spaced between 1 and 800 ms, and fraction resolution of  $\Delta\omega = 0.05$  for  $T_2 < 40 \text{ms}$  and  $\Delta\omega = 0.1$  for  $T_2 > 40 \text{ms}$ , producing 3,273,304  $\text{mcT}_2$  motifs. Initial fitting identified the specific range of single  $T_2$  values within each segment used it to exclude  $\text{mcT}_2$  motifs that do not fit into this range. Statistical correlations between simulated and experimental  $\text{mcT}_2$  signals ( $\text{Pr}(d,e)$ ) were normalized and raised by a power of  $\beta = 10^4$ . Global probability scores  $\text{Pr}(d)$  were computed, and a set of  $\text{mcT}_2$  motifs containing  $\mathcal{L} = 30$  dictionary elements with highest probabilities was selected. Table 1 lists the full set of parameters values. To compare the  $\text{mcT}_2$  content at  $T_2 > 40 \text{ms}$ , the geometric mean  $T_2$  (intra-/extra-axonal water  $T_2$ )<sup>11</sup> of the major component was calculated (mean on a logarithmic  $T_2$  scale). To demonstrate the potential of the proposed method to produce whole-brain MWF maps, the suggested data-driven algorithm was applied on the entire WM using the same  $\text{mcT}_2$  dictionary and parameter set (last row in Table 1). To appreciate the advantage of the data-driven approach, we compared the resulting map with a map that was generated using the standard voxel-wise NNLS fitting algorithm by Provencher.<sup>36</sup>

## 4 | RESULTS

### 4.1 | Numerical phantom results

Five representative  $\text{mcT}_2$  spectra containing 1, 2, and 3 sub-voxel components of a numerical phantom are shown in Figure 4, compared with ground truth (dashed and solid lines, respectively). Excellent reconstruction was achieved at  $\text{SNR} = 60$  for the 1, 2, and 3 compartment tissues, as well as for the inflamed tissue. The fitted intra-/extra-peak in Figure 4C was lower by 12% and broader by 4 ms compared to ground truth. This, however, did not affect the accuracy in detecting the myelin peak. The MWF map that was calculated by the suggested method perfectly matched the ground truth MWF map at  $\text{SNR} \geq 60$  as presented in Figure 3C, whereas at  $\text{SNR}$  of 40 it underestimated the two-compartment tissue (by factor of ~1/2) and misidentified the 0.2 myelin fraction in the three-compartment tissue (light-orange tissue in Figure 4). The MWF maps that were calculated using the voxel-wise NNLS fitting method are presented in Figure 5, exhibiting maps of lower quality. The map at  $\text{SNR} = 60$  shows a successful reconstruction of the myelin fraction in the single- and two-component tissue, together with a minor ~5% myelin overestimation in the three-compartment tissue. This fitting approach, however, misidentified the three-compartment tissue with 0.1 myelin fraction and all the lesioned voxels. At  $\text{SNR} = 25$ , both methods presented incorrect reconstruction.



**FIGURE 4**  $mcT_2$  fitting of numerical MESE phantom. (A–E) Fitted  $T_2$  distributions, i.e., spectra (dotted orange line), versus the ground truth (solid blue line) from noisy simulated MESE signals (SNR 60) showing excellent reconstruction of 1, 2, and 3 subvoxel compartments.  $T_2$  distributions are marked with matching segment colors as indicated

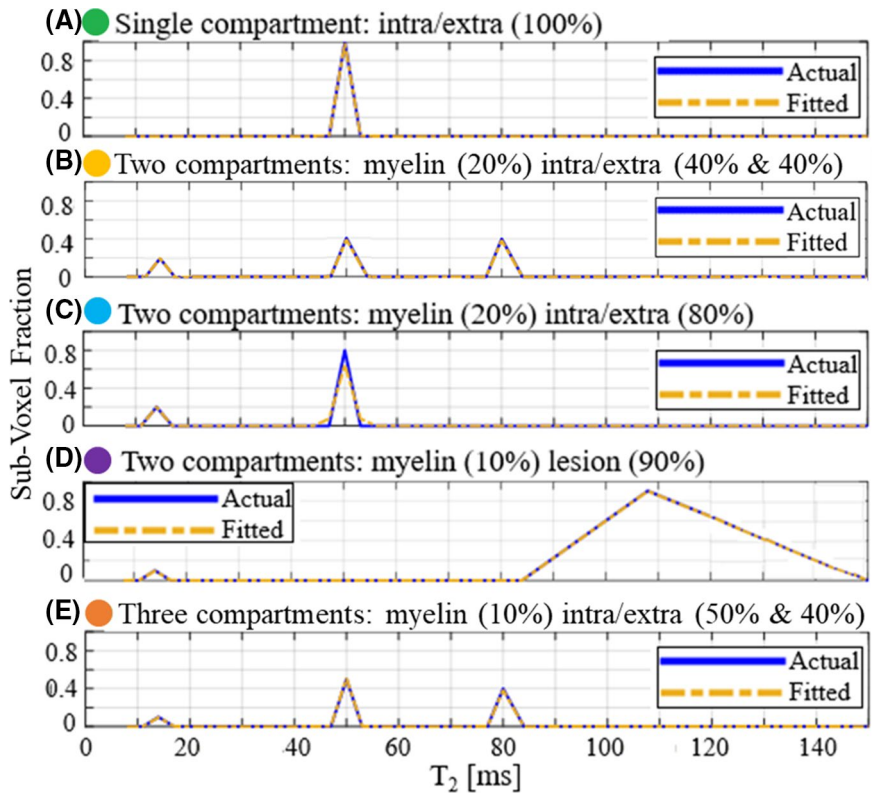
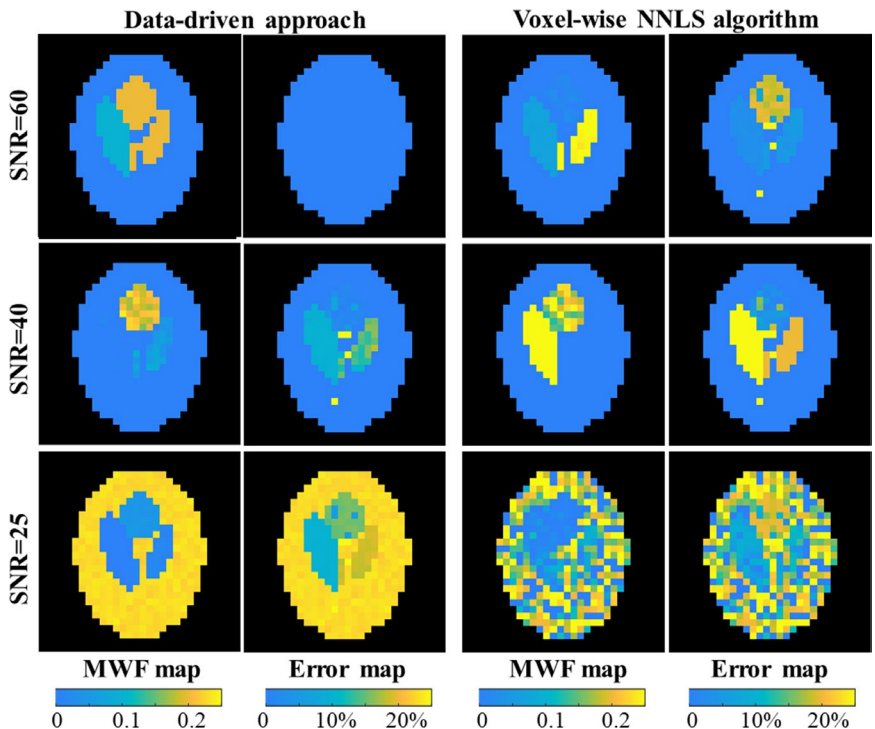


**FIGURE 5** Myelin water fraction maps estimations of numerical MESE phantom. Voxel-wise comparison of the reconstructed MWF values calculated with the proposed data-driven  $mcT_2$  algorithm and conventional voxel-wise non-negative least squares fitting.<sup>24,36</sup> Prior to the reconstruction, white Gaussian noise was added to the signals at varying SNR levels, and random  $T_2$  values in a range of  $\pm 20\%$  from the true  $T_2$  values were simulated within each segment. Error maps were calculated as the absolute difference between each map and the ground truth MWF map in Figure 3. MWF, myelin water fraction



## 4.2 | Experimental $mcT_2$ phantom

Representative high-resolution  $T_2$ -weighted images of the two-compartment phantoms are presented in Figure 6A wherein each  $T_2$  compartment is reflected as a different grayscale level. The figure shows the different phases of the experiment in which 1 mm tubes are gradually added

to the holding tube, producing ground-truth short  $T_2$  fractions of 0, 0.26, 0.44, and 0.66, denoted as MWF. Fitted MWF are shown versus the actual fractions in Figure 6B, producing a linear correlation with  $p < .01$  and  $r$  square of 0.99. Results for the three-compartment phantom are presented in Figure 6C,D. Baseline scan included only 2  $T_2$  compartments, 51 and 80 ms, after which short  $T_2$  tubes

were gradually added (small black circles), producing short  $T_2$  fractions of 0, 0.02, 0.04, 0.06, 0.08, 0.10, and 0.16 denoted as MWF. Fitted MWF are shown versus actual fractions in Figure 6 D, indicating high linear correlation with  $p < .001$  and  $r$  square of 0.99. Unlike Figure 6B, this correlation graph is based on a more complex structure with both 2 and 3  $T_2$  compartments. Both phantom designs produced correct baseline values, crossing the origin with no apparent bias.

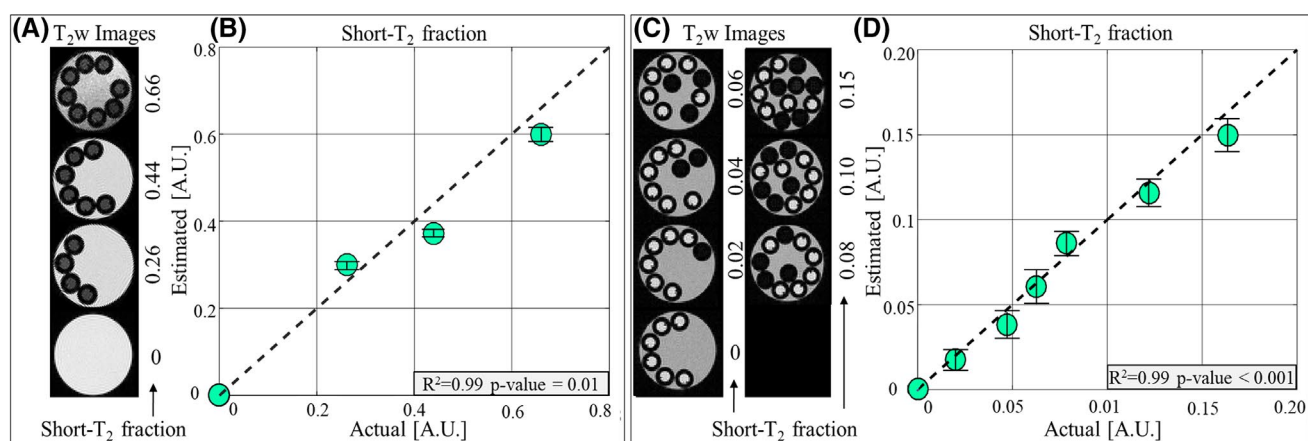
### 4.3 | mcT<sub>2</sub> of in vivo brain data

Figure 7 presents mcT<sub>2</sub> analysis of 3 WM segments: GCC, SCC, and left forceps minor. To validate repeatability, scan was repeated 3 consecutive times. MWF values for the left forceps minor GCC and SCC ranged between 10%–16%, 5%–12%, and 8%–14%. Average and SD MWF values are presented for each segment in Table 2. These values demonstrate an overlapping range of MWF values with similar means and relatively low SDs of 1.4% (GCC), 0.5% (SCC), and 1.0% (left forceps minor) across scans. The remaining  $T_2$  spectrum (i.e., at  $T_2 > 40$ ) was also consistent between scans, producing a similar geometric mean (intra-/extra-axonal water  $T_2$ ) and SDs (Table 2). The average single  $T_2$  values within the segments were almost identical between the 3 scans (GCC =  $49.9 \pm 0.8$  ms; SCC =  $57.2 \pm 2.1$  ms; left forceps minor =  $52.9 \pm 0.8$  ms), except for the second SCC scan for which values were lower by almost 4 ms

compared to the other 2 scans. Figure 8 shows whole-WM MWF maps that were obtained using the data-driven and the standard voxel-wise NNLS fitting algorithms. The data-driven approach produced a smoother MWF pattern compared to the standard voxel-wise approach, which exhibited a significant number of voxels for which the fitting process failed to identify any myelin (i.e., WM voxels indicating 0 value).

## 5 | DISCUSSION

Reliable mcT<sub>2</sub> analysis is highly challenging due to the large ambiguity in the mcT<sub>2</sub> search space, particularly when avoiding prior assumptions regarding the number or relaxation times of each compartments, leading to inconsistency of MWF value across different techniques.<sup>23</sup> This study introduces a new data-driven approach which starts by analyzing data from multiple voxels to extract spatially global mcT<sub>2</sub> motifs and only then uses these to locally analyze the signal at each voxel. This pre-processing learning stage promotes convergence while maintaining the sensitivity to subtle subvoxel changes. It assumes that voxels from a specific tissue segment contain a finite number of microstructural features that can be modeled using a finite set of mcT<sub>2</sub> motifs and thus does not require imposing a fixed number of  $T_2$  components or distributions. The presented global-to-local profiling of the tissue dramatically reduces the



**FIGURE 6** Validation of the new mcT<sub>2</sub> fitting algorithm on physiological subvoxel phantoms. (A,C) High-resolution scans of two- and three-compartment phantoms (FOV = 5 mm<sup>2</sup>) were used as ground truth for the subvoxel compartmentation. Each scan was performed at increased fractions of the short  $T_2$  compartment, resembling the brain MWF. (A) Two-compartment phantom:  $T_2$  of 11 and 60 ms for modeling myelin water (dark-gray circles) and intra-/extra-axonal water pools (light-gray background). (C) Three-compartment phantom:  $T_2$  of 11, 51, and 80 ms for modeling myelin water (black circles), intra-axonal (dark-gray background), and extra-axonal (light-gray circles) water pools. This unique phantom design provided the true ground truth fraction of the short  $T_2$  compartment. Experimental mcT<sub>2</sub> signals were acquired by capturing the entire phantom within a single voxel using a series of low-resolution scans ( $N_{\text{slices}} = 9$ ) (see Supporting Information Figure S1) with varying slice offsets. Acquired data were analyzed using the suggested mcT<sub>2</sub> algorithm. (B,D) Correlation between fitted and ground truth short  $T_2$  fractions, exhibiting an excellent agreement with  $r$  squares of 0.99, 0.99 and  $p$  values of .01, < .001 for the two- and three-compartment phantoms, respectively. Error bars indicate SDs of short  $T_2$  fractions across different slices

**FIGURE 7** Repeatability of the new  $mcT_2$  algorithm on in vivo brain data. Parametric maps of white matter segments from 3 consecutive scans of the same subject were used to test interscan stability of MWF values. (A–D) MWF maps of genu of corpus callosum. (E–H) MWF maps of splenium of corpus callosum. (I–K) MWF maps of the left forceps minor. MWF values are presented with the same color scale overlaid on a  $T_2$  map (gray scale)

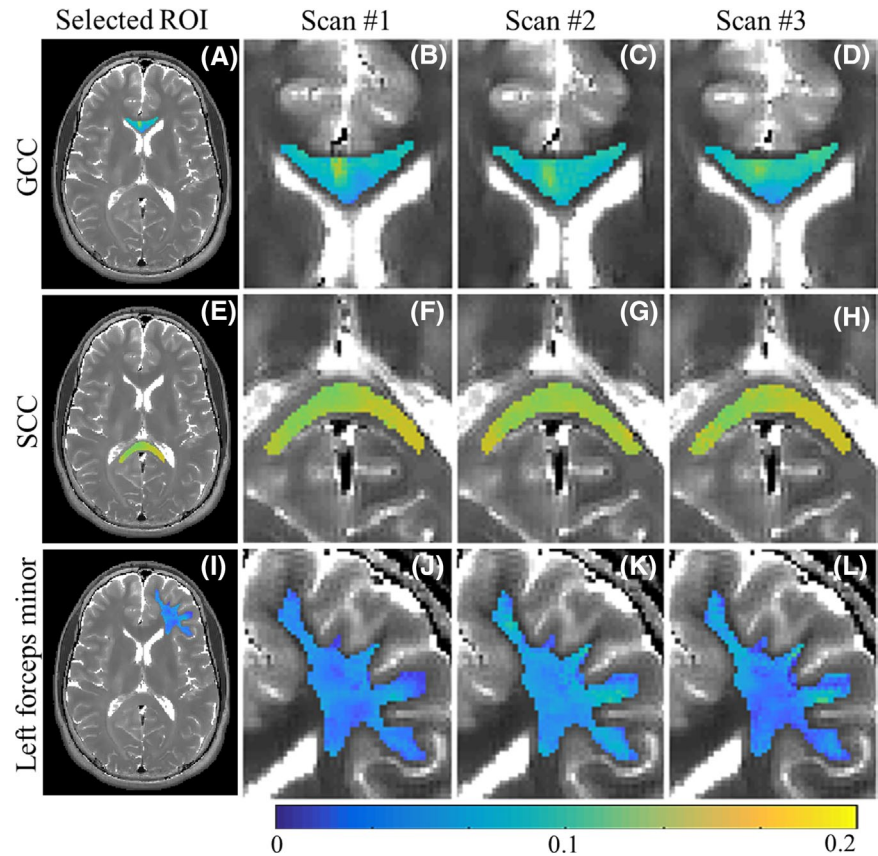


**TABLE 2** Distribution of  $mcT_2$  values estimated using the suggested algorithm from 3 consecutive scans of the same subject

WM segment	GCC			SCC			Left forceps minor		
	MWF (%)	IET <sub>2</sub> (ms)	T <sub>2</sub> (ms)	MWF (%)	IET <sub>2</sub> (ms)	T <sub>2</sub> (ms)	MWF (%)	IET <sub>2</sub> (ms)	T <sub>2</sub> (ms)
1st	9.5 ± 1.7	63.4 ± 0.9	50.5 ± 1.4	14.1 ± 0.6	80.4 ± 0.2	58.8 ± 3.9	8.6 ± 0.9	64.1 ± 1.8	52.9 ± 1.7
2nd	10.1 ± 1.0	63.3 ± 1.2	49.1 ± 1.5	14.0 ± 0.4	75.7 ± 0.2	54.8 ± 2.0	8.2 ± 1.0	64.4 ± 1.9	52.1 ± 1.9
3rd	10.2 ± 1.4	63.5 ± 1.1	50.1 ± 1.5	14.3 ± 0.6	78.6 ± 0.3	58.2 ± 2.3	7.8 ± 1.1	63.5 ± 1.7	53.7 ± 2.3

Abbreviations: GCC, genu of corpus callosum; IET<sub>2</sub>, intra-/extra-axonal water T<sub>2</sub> (mean ± SD); MWF, myelin water fraction (mean ± SD); SCC, splenium of corpus callosum; T<sub>2</sub>, signal T<sub>2</sub> value (mean ± SD); WM, white matter.

number of potential solutions, thereby addressing the inherent ill-posedness of  $mcT_2$  analysis. Unlike other data-driven approaches, which jointly estimate spectra of several voxels,<sup>37</sup> or those which utilize information across the entire image (such as the recent method proposed by Slator et al.<sup>38</sup>), the proposed method solves the  $mcT_2$  problem on a voxel-by-voxel basis using a typical linear matrix form (Equation 3). We therefore consider our technique a voxel-based approach. Its accuracy was demonstrated on a numerical phantom using a unique phantom design (with known ground truth) and in vivo on WM brain segments. Notwithstanding the promising results, further investigations are required to benchmark this approach and compare it to existing techniques.

### 5.1 | Novelty of the suggested $mcT_2$ algorithm

The suggested data-driven approach introduces 3 novel strategies for tackling the ambiguity in the  $mcT_2$  space. First, contrary to traditional approaches that describe the signals as a weighted combination of single-T<sub>2</sub> signals, it models them as a weighted combination of  $mcT_2$  motifs. This paradigm shift is beneficial for describing tissues based on realistic building blocks, each exhibiting a different microstructural compartmentation. Second, its method introduces a novel preprocessing stage in which global  $mcT_2$  motifs are derived from the anatomy and then used to locally analyze each voxel. This global-to-local strategy is highly efficient in reducing the number



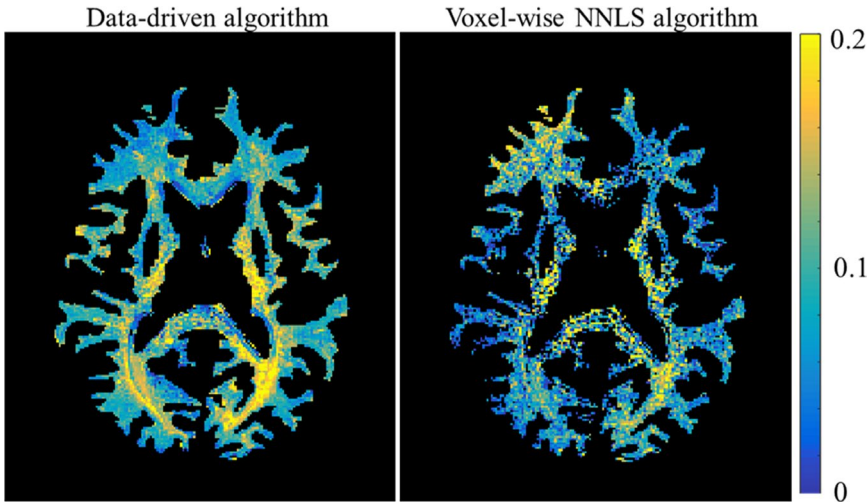


**FIGURE 8** Comparison of whole-white matter MWF maps generated using the proposed data-driven (left) and standard voxel-wise non-negative least squares fitting algorithm<sup>24,36</sup> (right). The data-driven preprocessing step affords improved stability and significantly fewer fitting errors

of possible solutions. In contrary to previous approaches for which all  $mcT_2$  configurations participate in the fitting process, the proposed strategy focuses the optimizer to identify the subset of  $mcT_2$  motifs that have the highest compatibility with the measured data. This reduces the chance of converging to unrealistic solutions, even if they present higher fitting accuracy at the pixel level. Third, the method is modular in a sense that it could easily be expanded to higher number of subvoxel compartments or focused at specific  $T_2$  ranges, thereby making it applicable to other tissues and pathologies. For example, modeling the cerebral spinal fluid compartment by adding a fourth, long  $T_2$  compartment or using a dictionary focused on higher  $T_2$  values to probe the gray matter compartmentation.

## 5.2 | Findings of the current study

The numerical simulations point out 2 major strengths of the suggested method. First, the successful reconstruction of spectra with 1, 2, and 3  $T_2$  compartments indicates that this data-driven approach can identify the correct number of  $T_2$  components without prior assumptions. This is particularly notable when analyzing voxels with only 1  $T_2$  component. In these voxels, the method did not fall short like classical fitting algorithms, which tend to improve accuracy by overfitting the signal to a larger number of components. Instead, it correctly identified the number of components and avoided the ambiguity in the signal space. Secondly, the perfect reconstruction at SNR of 60 and above demonstrates its robustness to noise. Such level of robustness was superior to the implemented voxel-wise NNLS fitting algorithm and comparable with the reported state-of-the-art  $mcT_2$  analysis methods.<sup>12,20,39-41</sup> More importantly, it implies the clinical potential of the suggested method.

In vivo validation of  $mcT_2$  fitting is challenging due to lack of ground truth. Correlations to histology were shown to provide some insight into microstructural features but are limited.<sup>4</sup> To generate ground truth data, we designed a unique multi- $T_2$  phantom with 2 distinct length scales and having both subvoxel morphology and internal modularity. Its dimensions were carefully selected to enable a low-resolution scan for which the entire phantom is captured in a single voxel (voxel size of  $5 \text{ mm}^2$ ), and a high-resolution scan that reflects its internal structure (voxel size of  $0.15 \text{ mm}^2$ ) and provides ground truth for the  $T_2$  values and relative fraction of each compartment. The global-to-local analysis requires a minimal number of voxels within the analyzed tissue segment to identify the global  $mcT_2$  motifs. We found this number to be around 100 voxels to achieve reliable profiling of the anatomy.

The modularity of the phantom design could be beneficial for modeling biological processes occurring at subvoxel levels. In this study, we used this ability to model myelination levels in the WM based on two- and three-compartment tissue model, showing high correlation between estimated and actual short- $T_2$  fractions. Moreover, the method was able to select the true number of compartments in 1, 2, or 3 compartments voxels without assuming a prior tissue compartmentation. This was seen in both phantom designs, implying the methods' reliability, particularly in the three-compartment phantom where 7 different levels of short  $T_2$  fractions were successfully recovered. Despite the accurate MWF estimation, we should remember that our phantom design does not consider intercompartmental water exchange that may impact MWF quantification.<sup>3</sup> Hence, future work needs to incorporate inter-compartmental exchange into the  $mcT_2$  dictionary simulations. The repeatability of the suggested approach was tested on 3 consecutive brain scans performed on the same subject in 1 session, producing consistent MWF values for each WM segment that coincide with values



reported in the literature.<sup>41</sup> Lastly, a proof-of-concept myelin mapping of the entire WM showed improved MWF quantification compared to standard voxel-wise NNLS fitting algorithm.<sup>36</sup>

### 5.3 | Clinical applicability

The subvoxel imaging ability of the suggested data-driven technique may serve as basis for several clinical applications, mainly for myelodegenerative diseases like multiple sclerosis, Alzheimer disease, and neuromyelitis,<sup>41</sup> for which a subvoxel information could improve the assessment of disease state compared to conventional contrast-weighted images. Another clinical use is for tracking changes in brain lipids content in aging-related conditions,<sup>42</sup> early detection of fat infiltration in muscle dystrophies,<sup>43,44</sup> accumulation of fat in the liver,<sup>45</sup> fat necrosis in breast tissue,<sup>46</sup> or characterization of the internal composition of cancerous tumors as shown in Ref.47. The ability to visualize these changes could potentially uncover subtle microstructural changes that are currently detectable only postmortem.

### 5.4 | Study limitations

Water exchange between microenvironments, such as the intra-/extracellular spaces, exists and may impact MWF quantification.<sup>3</sup> The suggested method, however, as well as similar NNLS-based methods, assume a slow exchange regime in which intercompartmental exchange occurs at slower time scales than the  $T_2$  relaxation time.<sup>15</sup> According to current reports, this assumption is valid in the WM, where the intraaxonal mean residence time are in the order of 100 s of ms<sup>48</sup> Because this assumption is not generally sustained, exchange might bias subvoxel analysis, requiring to expand our tissue model to incorporate exchange, for example, using Bloch-Torrey equations for 2 multi-compartment relaxation dynamics.<sup>49</sup>

For a successful reconstruction, the presented method needs to be applied on a single WM segment consisting of voxels with similar compartmentation. For this reason, in vivo MWF maps (e.g., in Figure 7) are shown for specific WM segments. To map the entire WM, the method should be applied consecutively, each time on data from a different WM segment, and only then combined to cover the entire WM. This limitation could be circumvented by analyzing multiple WM segments at the same time using parallel computing.

Modeling the internal structure of biological tissues is complex and may require more than 3 subvoxel compartments. Expansion of the suggested model to 4 or more compartments is possible but will dramatically increase

the size of the  $mcT_2$  dictionary, requiring stronger computation power than available on a standard personal computer. Another enhancement could be to expand the dynamic range and resolution of the  $T_2$  space to include denser  $T_2$  grids and improve the tissue modeling. Nevertheless, the use of such parsimonious dictionaries, which are tailored to the tissue in question, is common and has shown useful for  $mcT_2$  analysis.<sup>18</sup>

## 6 | CONCLUSION

This work presents a new data-driven approach for  $mcT_2$  analysis. The approach employs global statistical correlations to identify dominant  $mcT_2$  motifs, which are then used to constrain local analysis at the voxel level, while laying minimal a priori assumptions on the tissue microstructure.  $T_2$  relaxation curves were modeled using the EMC algorithm, ensuring stability across scanners and scan settings. This choice can be generalized to other signal models such as extended phase graph,<sup>39</sup> multiexponential decay, or MR fingerprinting.<sup>21</sup> Our findings on numerical and physical phantoms demonstrate the accuracy of the proposed  $mcT_2$  analysis. In vivo results demonstrate that MWF maps derived using this approach are repeatable and consistent with literature, implying its potential for MWI. No less important,  $T_2$  signals can be quantified within a clinical timescale, making the presented technique applicable for clinical applications. Full source code can be downloaded at <https://github.com/NBE-LAB/MCT2.git>.

### ORCID

Noam Ben-Eliezer  <https://orcid.org/0000-0003-2944-6412>

### REFERENCES

1. Lancaster JL, Andrews T, Hardies LJ, Dodd S, Fox PT. Three-pool model of white matter. *J Magn Reson Imaging*. 2003;17:1-10.
2. Mackay A, Whittall K, Adler J, Li D, Paty D, Graeb D. In vivo visualization of myelin water in brain by magnetic resonance. *Magn Reson Med*. 1994;31:673-677.
3. Alonso-Ortiz E, Levesque IR, Pike GB. MRI-based myelin water imaging: a technical review. *Magn Reson Med*. 2015;73:70-81.
4. Laule C, Kozlowski P, Leung E, Li DKB, MacKay AL, Moore GRW. Myelin water imaging of multiple sclerosis at 7 T: correlations with histopathology. *NeuroImage*. 2008;40:1575-1580.
5. West KL, Kelm ND, Carson RP, Gochberg DF, Ess KC, Does MD. Myelin volume fraction imaging with MRI. *NeuroImage*. 2018;182:511-521.
6. Laule C, Leung E, Li DK, et al. Myelin water imaging in multiple sclerosis: quantitative correlations with histopathology. *Mult Scler*. 2006;12:747-753.
7. Levesque IR, Giacomini PS, Narayanan S, et al. Quantitative magnetization transfer and myelin water imaging of the evolution of acute multiple sclerosis lesions. *Magn Reson Med*. 2010;63:633-640.

8. Billiet T, Vandenbulcke M, Mädler B, et al. Age-related microstructural differences quantified using myelin water imaging and advanced diffusion MRI. *Neurobiol Aging*. 2015;36:2107-2121.
9. Faizy TD, Thaler C, Broocks G, et al. The myelin water fraction serves as a marker for age-related myelin alterations in the cerebral white matter – a multiparametric MRI aging study. *Front Neurosci*. 2020;14:136.
10. Whittall KP, MacKay AL, Graeb DA, Nugent RA, Li DKB, Paty DW. In vivo measurement of T2 distributions and water contents in normal human brain. *Magn Reson Med*. 1997;37:34-43.
11. Deoni SCL. Quantitative relaxometry of the brain. *Top Magn Reson Imaging*. 2010;21:101-113.
12. Does MD. Inferring brain tissue composition and microstructure via MR relaxometry. *NeuroImage*. 2018;182:136-148.
13. MacKay AL, Laule C. Magnetic resonance of myelin water: an in vivo marker for myelin. *Brain Plast*. 2016;2:71-91.
14. Vavasour IM, Laule C, Li D, et al. Longitudinal changes in myelin water fraction in two MS patients with active disease. *J Neurol Sci*. 2009;276:49-53.
15. Gareau PJ, Rutt BK, Karlik SJ, Mitchell JR. Magnetization transfer and multicomponent T2 relaxation measurements with histopathologic correlation in an experimental model of MS. *J Magn Reson Imaging*. 2000;11:586-595.
16. Bouhrara M, Reiter DA, Bergeron CM, et al. Evidence of demyelination in mild cognitive impairment and dementia using a direct and specific magnetic resonance imaging measure of myelin content. *Alzheimer's Dement*. 2018;14:998-1004.
17. Prasloski T, Rauscher A, MacKay AL, et al. Rapid whole cerebrum myelin water imaging using a 3D GRASE sequence. *NeuroImage*. 2012;63:533-539.
18. Deoni SCL, Rutt BK, Arun T, Pierpaoli C, Jones DK. Gleaning multicomponent T1 and T2 information from steady-state imaging data. *Magn Reson Med*. 2008;60:1372-1387.
19. Bouhrara M, Spencer RG. Improved determination of the myelin water fraction in human brain using magnetic resonance imaging through Bayesian analysis of mcDESPOT. *NeuroImage*. 2016;127:456-471.
20. Ma D, Gulani V, Seiberlich N, et al. Magnetic resonance fingerprinting. *Nature*. 2013;495:187-192.
21. Bipin Mehta B, Coppo S, Frances McGivney D, et al. Magnetic resonance fingerprinting: a technical review. *Magn Reson Med*. 2019;81:25-46.
22. Zhang J, Kolind SH, Laule C, Mackay AL. Comparison of myelin water fraction from multiecho T2 decay curve and steady-state methods. *Magn Reson Med*. 2015;73:223-232.
23. West DJ, Teixeira RPAG, Wood TC, Hajnal JV, Tournier JD, Malik SJ. Inherent and unpredictable bias in multi-component DESPOT myelin water fraction estimation. *NeuroImage*. 2019;195:78-88.
24. Whittall KP, MacKay AL. Quantitative interpretation of NMR relaxation data. *J Magn Reson*. 1989;84:134-152.
25. Whittall KP. Recovering compartment sizes from NMR relaxation data. *J Magn Reson*. 1991;94:486-492.
26. Saab G, Thompson RT, Marsh GD. Multicomponent T2 relaxation of in vivo skeletal muscle. *Magn Reson Med*. 1999;1:150-157.
27. Björk M, Zachariah D, Kullberg J, Stoica P. A multicomponent T2 relaxometry algorithm for myelin water imaging of the brain. *Magn Reson Med*. 2016;75:390-402.
28. Akhondi-Asl A, Afacan O, Mulkern RV, Warfield SK. T2-relaxometry for myelin water fraction extraction using Wald distribution and extended phase graph. *Lect Notes Comput Sci*. 2014;8675:145-152.
29. Graham SJ, Stanchev PL, Bronskill MJ. Criteria for analysis of multicomponent tissue T2 relaxation data. *Magn Reson Med*. 1996;35:370-378.
30. Ben-Eliezer N, Sodickson DK, Block KT. Rapid and accurate T2 mapping from multi-spin-echo data using Bloch-simulation-based reconstruction. *Magn Reson Med*. 2015;73:809-817.
31. Ben-Eliezer N, Sodickson DK, Shepherd T, Wiggins GC, Block KT. Accelerated and motion-robust in vivo T2 mapping from radially undersampled data using Bloch-simulation-based iterative reconstruction. *Magn Reson Med*. 2016;75:1346-1354.
32. Radunsky D, Stern N, Nassar J, Tsarfaty G, Blumenfeld-Katzir T, Ben-Eliezer N. Quantitative platform for accurate and reproducible assessment of transverse (T2) relaxation time. *NMR Biomed*. 2021;34:1-14.
33. MacKay A, Laule C, Vavasour I, Bjarnason T, Kolind S, Mädler B. Insights into brain microstructure from the T2 distribution. *Magn Reson Imaging*. 2006;24:515-525.
34. Neta S, Radunsky D, Blumenfeld-Katzir Tamar T, Ben-Eliezer N. Accurate mapping of T2 relaxation times at low SNR, based on Bloch simulations and PCA image denoising. In ISMRM 20 Digital Posters Page: Contrast Mechanisms: Quantitative Tissue Properties and Novel Contrast Mechanisms; 2020. E-poster 5605. Abstract 3240. <https://archive.ismrm.org/2020/3240.html>. Accessed May 20, 2021.
35. Gudbjartsson H, Patz S. The Rician distribution of noisy MRI data. *Magn Reson Med*. 1995;34:910-914.
36. Provencher SW. A constrained regularization method for inverting data represented by linear algebraic or integral equations. *Comput Phys Commun*. 1982;27:213-227.
37. Kim D, Doyle EK, Wisnowski JL, Kim JH, Haldar JP. Diffusion-relaxation correlation spectroscopic imaging: a multidimensional approach for probing microstructure. *Magn Reson Med*. 2017;78:2236-2249.
38. Slator PJ, Hutter J, Marinescu RV, et al. Data-driven multi-contrast spectral microstructure imaging with InSpect: INtegrated SPECTral component estimation and mapping. *Med Image Anal*. 2021;71:e102045.
39. Prasloski T, Mädler B, Xiang QS, MacKay A, Jones C. Applications of stimulated echo correction to multicomponent T2 analysis. *Magn Reson Med*. 2012;67:1803-1814.
40. Zhang J, Kolind SH, Laule C, MacKay AL. How does magnetization transfer influence mcDESPOT results? *Magn Reson Med*. 2015;74:1327-1335.
41. Lee J, Hyun J-W, Lee J, et al. So you want to image myelin using MRI: an overview and practical guide for myelin water imaging. *J Magn Reson Imaging*. 2021;53:360-373.
42. Filo S, Shtangel O, Salamon N, et al. Disentangling molecular alterations from water-content changes in the aging human brain using quantitative MRI. *Nat Commun*. 2019;10:3403.
43. Jo CH, Shin JS. Changes in appearance of fatty infiltration and muscle atrophy of rotator cuff muscles on magnetic resonance imaging after rotator cuff repair: establishing new time-zero traits. *Arthrosc: J Arthrosc Relat Surg*. 2013;29:449-458.
44. Amer R, Nassar J, Bendahan D, Greenspan H, Ben-Eliezer N. Automatic segmentation of muscle tissue and inter-muscular fat in thigh and calf MRI images. In: Shen D, Liu T, Peters TM, et al. eds. *Medical Image Computing and Computer Assisted Intervention – MICCAI 2019. Lecture Notes in Computer Science, Vol. 11765*. Springer; 2019:219-227. <https://arxiv.org/abs/1910.04866>. Accessed October 1, 2019.

45. Tang AN, Tan J, Sun M, et al. Nonalcoholic fatty liver disease: MR imaging of liver proton density fat fraction to assess hepatic steatosis. *Radiology*. 2013;267:422-431.
46. Fernandes Chala L, de Barros N, de Camargo Moraes P, et al. Fat necrosis of the breast: mammographic, sonographic, computed tomography, and magnetic resonance imaging findings. *Curr Probl Diagn Radiol*. 2004;33:106-126.
47. Storås TH, Gjesdal KI, Gadmar ØB, Geitung JT, Kløw NE. Prostate magnetic resonance imaging: multiexponential T2 decay in prostate tissue. *J Magn Reson Imaging*. 2008;28:1166-1172.
48. Nilsson M, Lätt J, van Westen D, et al. Noninvasive mapping of water diffusional exchange in the human brain using filter-exchange imaging. *Magn Reson Med*. 2013;69:1573-1581.
49. Magin RL, Abdullah O, Baleanu D, Zhou XJ. Anomalous diffusion expressed through fractional order differential operators in the Bloch-Torrey equation. *J Magn Reson*. 2008;190:255-270.

### SUPPORTING INFORMATION

Additional supporting information may be found in the online version of the article at the publisher's website.

**Data S1** Data-driven algorithm for myelin water imaging: Probing subvoxel compartmentation based on identification of spatially global tissue features

**Data S2** Numerical phantom simulation

**Data S3** Implementation of traditional voxelwise NNLS fitting algorithm

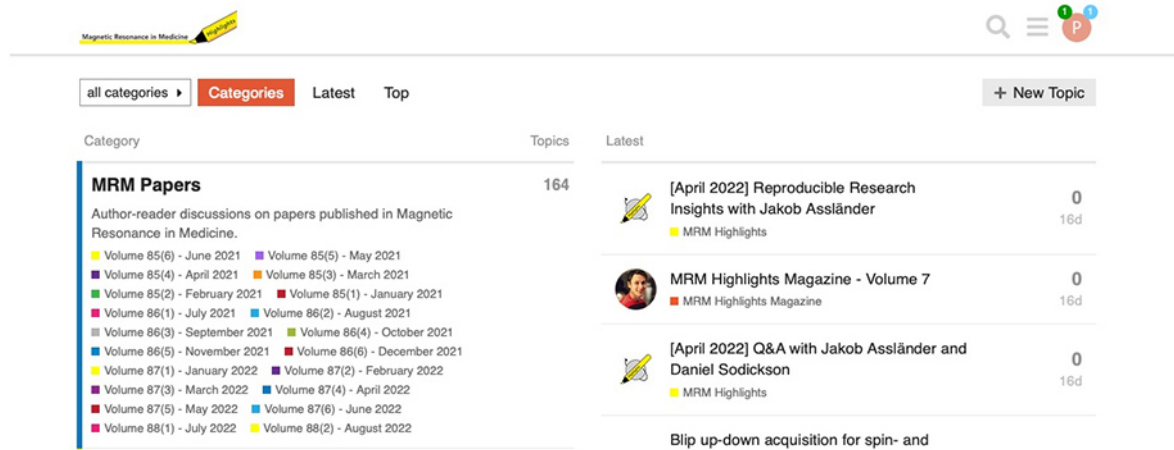
**Data S4** Design of sub-voxel phantom

**FIGURE S1** Validation of the  $mcT_2$  algorithm on a physiological sub-voxel phantom

**How to cite this article:** Omer N, Galun M, Stern N, Blumenfeld-Katzir T, Ben-Eliezer N. Data-driven algorithm for myelin water imaging: Probing subvoxel compartmentation based on identification of spatially global tissue features. *Magn Reson Med*. 2022;87:2521–2535. doi:[10.1002/mrm.29125](https://doi.org/10.1002/mrm.29125)

# WOULD YOU LIKE TO POST AN INFORMAL COMMENT ABOUT THIS PAPER, OR ASK THE AUTHORS A QUESTION ABOUT IT?

If so, please visit <https://mrm.ismrm.org/> and register for our Magn Reson Med Discourse site (registration is free).



The screenshot shows the Magn Reson Med Discourse website. At the top, there is a search bar and a navigation menu with 'all categories', 'Categories', 'Latest', and 'Top'. Below this, there is a 'New Topic' button. The main content area is divided into three columns: 'Category', 'Topics', and 'Latest'. The 'Category' column lists 'MRM Papers' with a description and a list of volume and issue information. The 'Topics' column shows '164' topics. The 'Latest' column displays three recent topics: '[April 2022] Reproducible Research Insights with Jakob Assländer', 'MRM Highlights Magazine - Volume 7', and '[April 2022] Q&A with Jakob Assländer and Daniel Sodickson'. Each topic includes a small icon, a title, a user profile picture, and a '0' comment count.

Magn Reson Med is currently listing the top 8 downloaded papers from each issue (including Editor's Picks) for comments and questions on the Discourse web site.

However, we are happy to list this or any other papers (please email [mrm@ismrm.org](mailto:mrm@ismrm.org) to request the posting of any other papers.)

We encourage informal comment and discussion about Magn Reson Med papers on this site. Please note, however, that a formal errata from the authors should still be submitted in the usual way via our Manuscript Central online submission system.